AGU PUBLICATIONS

Geophysical Research Letters

RESEARCH LETTER
10.1002/2017GL075641

Key Points:
- First observations of Antarctic short-period eastward propagating PWs with coherent phase structure in a large vertical extent (30-110 km) are reported
- New discovery of significant wave amplitude growth above 100 km suggests a third (second) amplitude peak in temperature (geopotential)
- A "seeding-amplification" mechanism of surviving PWs being amplified by in situ instability in the MLT is proposed to explain wave features

Correspondence to:
X. Lu and X. Chu,
xianl@clemson.edu;
xinzhao.chu@colorado.edu

Citation:
Lu, X., Chu, X., Chen, C., Nguyen, V., & Smith, A. K. (2017). First observations of short-period eastward propagating planetary waves from the stratosphere to the lower thermosphere (110 km) in winter Antarctica. *Geophysical Research Letters*, *44*, 10,744–10,753. https://doi.org/10.1002/2017GL075641

Received 12 SEP 2017
Accepted 10 OCT 2017
Accepted article online 13 OCT 2017
Published online 28 OCT 2017

First Observations of Short-Period Eastward Propagating Planetary Waves From the Stratosphere to the Lower Thermosphere (110 km) in Winter Antarctica

Xian Lu[1,2], Xinzhao Chu[1,3], Cao Chen[1,3], Vu Nguyen[3], and Anne K. Smith[4]

[1]Cooperative Institute for Research in Environmental Sciences, University of Colorado Boulder, Boulder, CO, USA, [2]Department of Physics and Astronomy, Clemson University, Clemson, SC, USA, [3]Department of Aerospace Engineering Sciences, University of Colorado Boulder, Boulder, CO, USA, [4]Atmospheric Chemistry Observations and Modeling, National Center for Atmospheric Research, Boulder, CO, USA

Abstract Unique Fe lidar observations in May 2014 at McMurdo, combined with Aura-Microwave Limb Sounder measurements, lead to a new discovery that the amplitudes of 4 day and 2.5 day planetary waves (PWs) grow rapidly from 1–2 K at 100 km to over 10 K at 110 km. This report is also the first observation of short-period (1–5 days) eastward propagating PWs from 30 km all the way to 110 km. The Specified Dynamics-Whole Atmosphere Community Climate Model reproduces the observed three dominant peaks of amplitudes in temperature and coherent vertical phase structures. The data-model comparison indicates a possible mechanism: After PWs originated from the stratosphere dissipate along the critical level, the surviving waves are amplified by in situ instability in the mesosphere and lower thermosphere, resulting in the second (third) peak in geopotential (temperature). This third peak in temperature explains the PW amplitude growth from 100 to 110 km.

1. Introduction

Planetary waves (PWs) propagating eastward relative to the ground with periods of 1–5 days and zonal wave numbers of 1–3 have been well observed in the winter polar stratosphere and mesosphere (e.g., Allen et al., 1997; Baumgaertner et al., 2008; Coy et al., 2003; Fraser et al., 1993; Garcia et al., 2005; Lawrence et al., 1995; Lu et al., 2013; Manney et al., 1998; Manney & Randel, 1993) but very rarely in the lower thermosphere, especially above 100 km. These waves are seen as strong perturbations in temperatures and horizontal winds and play important roles in the transport of momentum, heat, and chemical species. In the current study we report the first observations of eastward propagating PWs with periods of 1–5 days in Antarctica from the stratosphere to the lower thermosphere (110 km) via combined lidar and Microwave Limb Sounder (MLS) temperature measurements. In addition to a double-peak structure in the stratospheric and mesospheric temperature amplitudes of a 4-day wave, the lidar data show significant increases of wave amplitudes above 100 km, implying an extra peak in the lower thermosphere, which has not been reported previously to our knowledge. The Specified Dynamics-Whole Atmosphere Community Climate Model (SD-WACCM) (Kunz et al., 2011; Smith et al., 2017) qualitatively captures the vertical and latitudinal structures of the 4-day wave and therefore is applied to examine possible origins of PWs in the mesosphere and lower thermosphere (MLT).

Studies by Hartmann (1983), Manney and Randel (1993), and Watanabe et al. (2009) have shown that the stratospheric traveling PWs are generated from the barotropic/baroclinic instability of the polar night jet, which is characterized by a negative meridional gradient of potential vorticity (PV). Such generation is achieved as certain wave modes are amplified (i.e., possessing positive growth rates) by extracting energy from background mean flow and ultimately becoming the dominant waves (Hartmann, 1983). These eastward propagating PWs are confined to high latitudes in the winter stratosphere where they propagate westward relative to the strong eastward background winds. As the speed of the mean wind becomes weaker toward low latitudes, the refractive index becomes imaginary, preventing equatorward wave propagation (Lu et al., 2013). Similarly, as the PWs propagate from the stratosphere to the MLT, the eastward jet closes and the wind turns westward. A critical level where the wave's phase speed equals the mean wind should be encountered, preventing upward wave propagation (Matsuno, 1970). Therefore, direct and free wave propagation from the stratosphere to the lower thermosphere becomes less favorable, and the origin of PWs above 100 km in both lidar and SD-WACCM deserves investigation. Modeling studies by McLandress

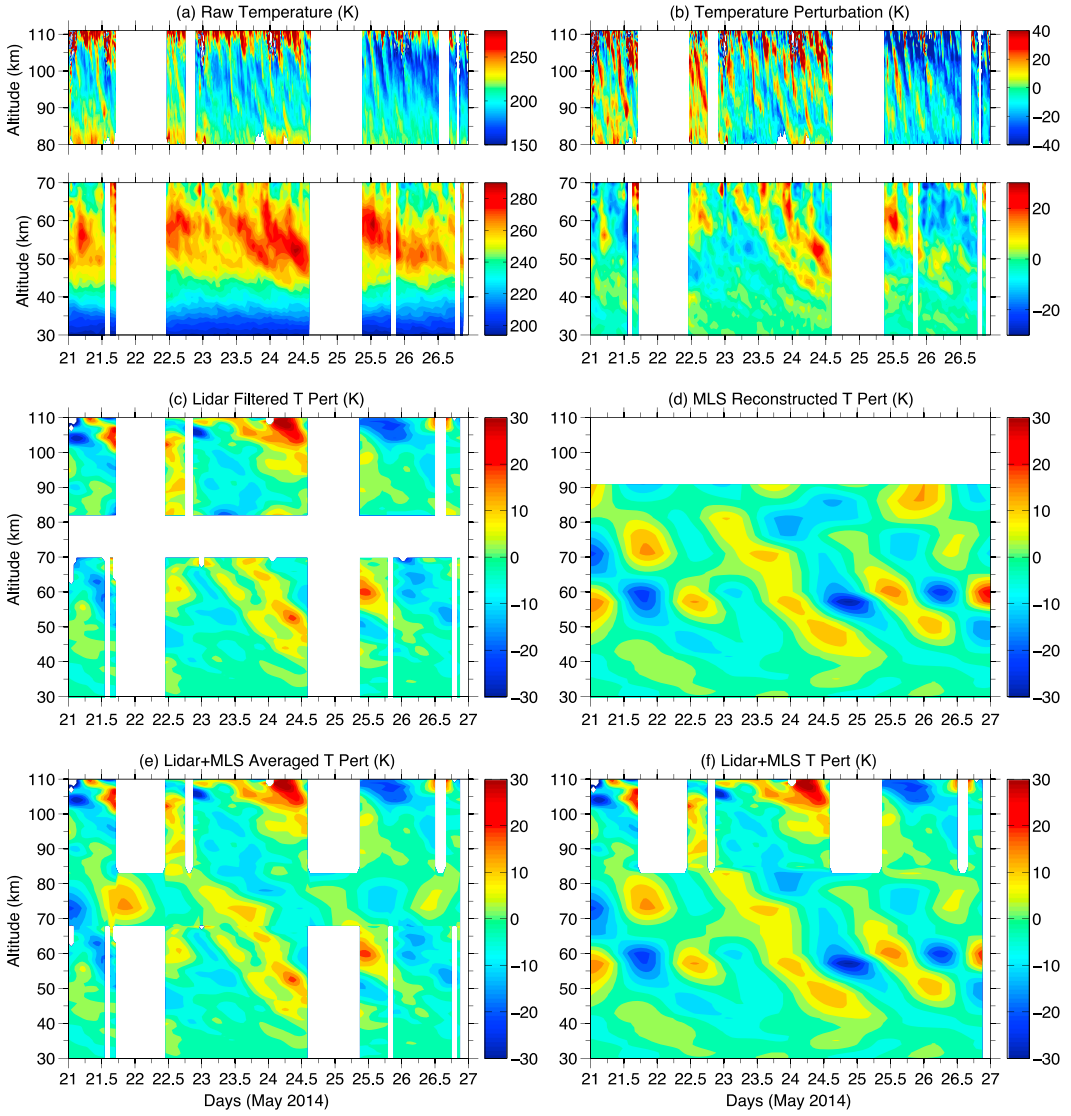

Figure 1. (a) Lidar temperatures from 21 to 26 May 2014 in the region of 30–110 km at McMurdo. (b) Temperature perturbations after subtracting the data set mean and a linear trend. (c) Low-pass-filtered temperature perturbations with a cutoff frequency of 12 h^{-1}. (d) MLS reconstructed temperature perturbations with major components of 4dE1, 2.5dE1, and 1.7dE2 waves. (e) Same as Figure 1c except that MLS reconstructed perturbations are fed into 68–84 km. (f) Same as Figure 1d except that lidar temperature perturbations are superimposed above 84 km.

et al. (2006) and Sato and Nomoto (2015) propose in situ instability as the wave source for mesospheric PWs, although the processes that lead to the unstable state are different. McLandress et al. (2006) suggest that the instability is caused by the gravity wave (GW)-induced wind shears in the mesosphere, while Sato and Nomoto (2015) suggest that associated with the poleward and downward shift of the polar night jet, westward GW forcing filtered by the eastward jet shifts accordingly and forms an upwelling motion that decreases temperature and increases static stability at midlatitudes. This process produces a negative PV gradient at high latitudes and gives rise to instability. Both papers solicit observational studies to confirm their hypotheses, and the current study provides evidence that the eastward PWs do attain substantial magnitudes in the MLT.

2. Lidar Observations and Results

The University of Colorado lidar group has been conducting lidar observations at Arrival Heights (77.83°S, 166.67°E) near McMurdo, Antarctica, since December 2010 (Chu, Huang, et al., 2011; Chu, Yu, et al., 2011).

The Fe Boltzmann lidar deployed in the campaign is capable of temperature measurements during both day and night, leading to full diurnal data coverage (Chu et al., 2002; Wang et al., 2012). Temperatures were derived from 30 to 70 km using Rayleigh integration technique and from 80 to 110 km using Fe Boltzmann technique (Fong et al., 2014; Lu et al., 2015). A gap between 70 and 80 km exists because neither the Rayleigh nor Fe signal level is sufficient to derive accurate temperatures. The raw lidar photon counts were recorded with resolutions of 1 min and 48 m. In order to reduce the photon noise-induced errors, we use resolutions of 1 h × 0.96 km in the Rayleigh region to deduce temperatures. The Fe temperatures are derived with resolutions of 0.25 h and 0.5 km and oversampled to 0.1 h and 0.1 km. Figure 1a shows the unique 6 day temperature measurements under these resolutions from 21 to 26 May 2014. Such a long and nearly continuous data set is optimal for the PW study.

We obtain temperature perturbations by subtracting the data set mean temperature and then applying a linear detrending at each altitude (Figure 1b). Perturbations with PW periods are obvious in the upper stratosphere and lower mesosphere (40–70 km). Although persistent inertia gravity waves (IGWs) with periods of 3–10 h are dominant in the MLT (Chen & Chu, 2017; Chen et al., 2013, 2016), PW periods are still noticeable by eye. For instance, warm temperatures around 100 km are observed from day ~22 to 23, which are replaced by cold temperatures from day 23 to 24. Warm temperatures occur again until nearly day ~26, after which cold temperatures start to reappear.

In order to be consistent with the Rayleigh region, Fe temperature data are further binned in intervals of 1 h × 0.96 km. Under this resolution, the measurement uncertainty of a single profile of the Rayleigh data ranges from ~0.1 K at 30 km to ~5 K at 65 km, and that of the Fe data ranges from ~0.2 K at 83 km to ~2 K at 110 km. A low-pass filter with a cutoff frequency of 12 h^{-1} is then used to suppress the strong IGWs in both regions which can also effectively suppress the measurement uncertainties by about 1 order of magnitude, leading to the uncertainties of ~0.02–0.5 K in the range of 30–65 km and ~0.02–0.25 K in 83–110 km. The Monte Carlo method used in Zhao et al. (2017) to derive the spectral noise floor of temperature perturbations is adopted here to estimate the uncertainties of temperature perturbations after filtering. The low-pass-filtered temperature perturbations (Figure 1c) show PW-period oscillations with 10–30 K amplitudes present all the way from the stratosphere to the MLT. These low-pass-filtered temperature perturbations are eventually used to derive wave amplitudes and phases in section 3.2. Since the low-pass-filtered temperature uncertainties are negligible, their contributions are not considered into the calculation of wave amplitude and phase uncertainties.

As a few data gaps exist in the lidar measurements, the Lomb-Scargle (LS) periodogram (Scargle, 1982) is used to identify the dominant wave components (Figure 2a). The LS spectra in wave amplitudes exhibit three dominant peaks at ~0.2–0.25, 0.4, and 0.6 day^{-1}, corresponding to ~4–5-day, 2.5-day, and 1.7-day waves, respectively. The substantial spectral amplitudes are mostly seen above 40 km, consistent with the location where the waves are excited by the polar night jet instability (Lu et al., 2013). The amplitude spectra averaged in the range of 45–90 km and 45–110 km also illustrate these three distinct spectral peaks (Figure 2b). The 4–5-day and 2.5-day waves grow significantly, while the 1.7-day wave weakens above 100 km; as a result the mean spectra of the former two waves are larger in the range of 45–110 km than 45–90 km, while the 1.7-day wave shows an opposite situation (Figure 2b).

3. Wave Components From MLS and Combined Wave Fields

3.1. MLS Spectral Analyses and Reconstruction of PWs

During the lidar observation period, Aura-MLS measurements (Schoeberl et al., 2006) have a good conjunction with McMurdo. The vertical resolution of the MLS data is ~1 km in 24–43 km, ~3 km in 46–60 km, and ~5 km in 66–91 km. The simultaneous MLS observations have global coverage of temperature measurements, enabling us to identify the wave propagation directions and zonal wave numbers. The fast Fourier synoptic mapping (FFSM) method (Salby, 1982) is used to compute the frequency × zonal wave number spectrum from Aura-MLS temperatures observed at each latitude × altitude grid point from 17 May to 2 June 2014. The latitude grid chosen is a 5° box centered around 77.5°S, and the longitudes chosen are from −180° to 180°, as long as they fall into this latitudinal box. Figure 2c shows the normalized FFSM amplitude spectra averaged in the altitude range of 45–90 km. Similar peaks at ~0.25, ~0.4, and ~0.6 day^{-1} in the frequency domain compared with the lidar results are identified from the FFSM mean spectra. The first two

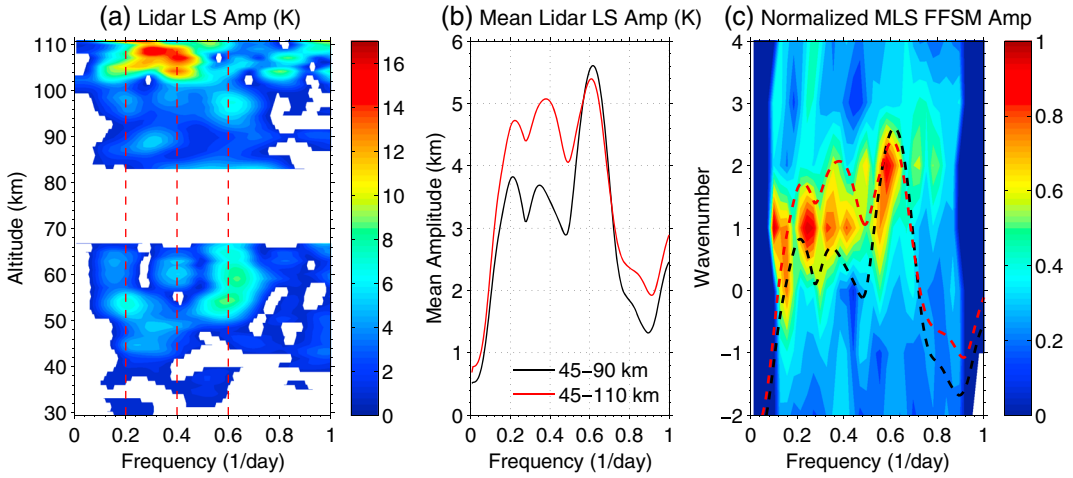

Figure 2. (a) Lidar LS amplitude spectra of the filtered temperature perturbations with confidence level of 95% and amplitude of 1 K as thresholds (b) mean lidar LS amplitude spectra averaged in the range of 45–90 km (black) and 45–110 km (red), respectively. (c) MLS normalized FFSM amplitude spectra averaged in the range of 45–90 km at 77.5°S. The averaged lidar spectra of Figure 2b are overplotted in Figure 2c as dashed lines with a vertical displacement of −3. Positive wave number corresponds to eastward propagating.

peaks propagate eastward with zonal wave number 1 and the third peak propagates eastward with zonal wave number 2.

The derived complex spectral coefficients from the FFSM are then used to reconstruct the temperature perturbations over McMurdo by selecting the longitude to be 166.7°E. Spectral coefficients observed at frequencies less than 0.1 day^{-1} and greater than 0.9 day^{-1} are not included in the reconstruction in order to mitigate the influence of stationary PWs and diurnal tides. The reconstructed MLS temperature perturbations (Figure 1d) well resemble the lidar-measured temperature perturbations (Figure 1c), which strongly suggests that the dominant peaks identified from the MLS spectra and from lidar are the same waves. According to the FFSM spectra, the major contributions to the reconstructed fields at McMurdo originate from the three dominant waves with frequencies of ~(0.25, 0.4, and 0.6) day^{-1} and eastward wave numbers of (1, 1, and 2), respectively. For simplicity, we refer to them as 4 day E1 (4dE1), 2.5dE1, and 1.7dE2 waves.

The lidar observations have a gap at 70–80 km, while the MLS data cease at 90 km. These two data sets are therefore combined to examine the continuous vertical structure of the dominant waves. Figure 1f shows a simple combination by superimposing the lidar data above 84 km on top of the MLS data below 84 km. Since the lidar data have higher vertical resolution than MLS, in Figure 1e, we retain the lidar measurements but sandwich the MLS-reconstructed temperature perturbations into the lidar gap region of 68–84 km. At the two boundaries (i.e., 68–70 km and 82–84 km), the MLS and lidar data are averaged to form smoother transitions. It is clear that the MLS reconstructed perturbations fit well into the lidar data patterns and the downward phase progressions are observed in the combined temperature fields (Figure 1e).

3.2. Vertical Structure of Wave Amplitudes and Phases

Figures 1 and 2 demonstrate that the same dominant waves are identified from the LS and FFSM spectra and the combined temperature fields produce coherent structures. We fit equation (1) to the temperature perturbations $T'(t,z)$ in Figure 1e to derive wave amplitudes and phases:

$$T'(t,z) = A_1(z)\cos[\omega_1(t-\varphi_1(z))] + A_2(z)\cos[\omega_2(t-\varphi_2(z))] + A_3(z)\cos[\omega_3(t-\varphi_3(z))], \quad (1)$$

where ($\omega_1, \omega_2,$ and ω_3) correspond to wave frequencies (0.25, 0.4, and 0.6) day^{-1} and ($A_1, A_2,$ and A_3) and ($\varphi_1, \varphi_2,$ and φ_3) are the respective wave amplitudes and phases. The wave amplitudes of the relative temperature perturbations, defined as the absolute temperature perturbations divided by the data set mean temperature $\overline{T}(z)$, are computed as $A_i(z)/\overline{T}(z)$ for the lidar data. The wave phase is defined as the universal time at which the maximum temperature perturbation is reached.

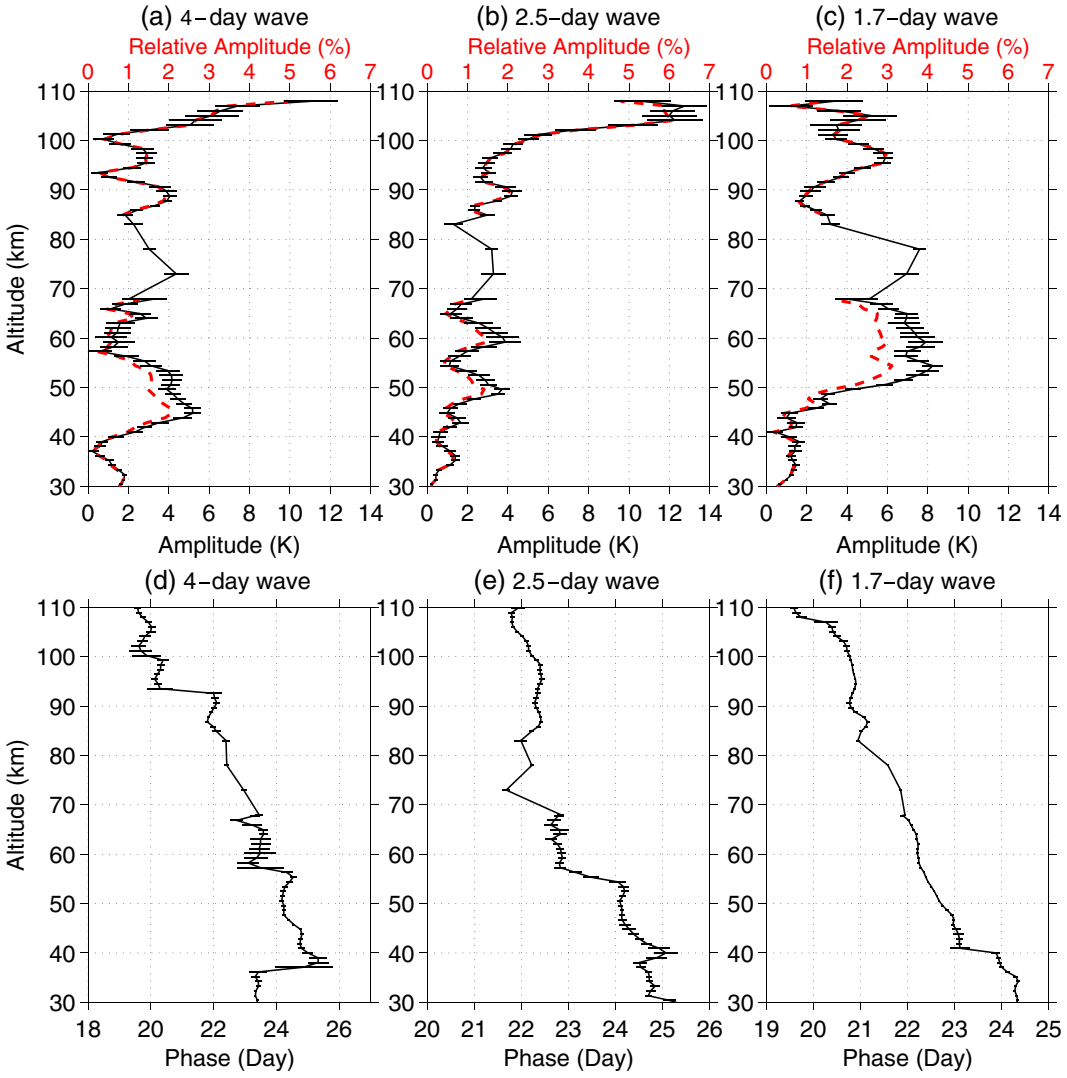

Figure 3. (a–c) Lidar amplitude profiles of the 4 day, 2.5 day, and 1.7-day waves for absolute (black) and relative (red) temperature perturbations. (d–f) Same as Figures 3a–3c except for wave phases. Error bars denote the uncertainties from sinusoidal fittings. The results of 68–84 km are from the MLS.

Figure 3 shows the vertical profiles of both absolute and relative wave amplitudes and phases. Note that there are several altitudes where all three waves reach large amplitudes. The first common peak is found near 50 km, and the secondary one is in the range of 70–80 km. There is one local minimum in between for the 4-day and 1.7-day waves and two local minima for the 2.5-day wave. This double-peak structure of the 4-day wave amplitude in temperature is consistent with satellite observations at wintertime high latitudes in the Northern Hemisphere (Garcia et al., 2005). From the hydrostatic balance for wave perturbations, that is, the vertical gradient of geopotential perturbations in the isobaric coordinate is proportional to temperature perturbations (Andrews et al., 1987, equation (3.4.2c)), a peak amplitude in geopotential perturbation at 60–70 km is where its gradient reaches zero, thereby corresponding to a minimum amplitude in temperature perturbation. Meanwhile, above and below this peak where the gradient of geopotential amplitude is the biggest, the wave amplitude in temperature perturbation reaches maximum, resulting in a double-peak structure.

A novel feature is that the 4-day and 2.5-day wave amplitudes increase significantly and reach ~10 K above 100 km, implying another peak in the thermosphere. Such amplitude increases are present in both absolute and relative temperatures, which demonstrate that these growths are independent of background

temperatures. The amplitude of the 1.7-day wave does not increase above 100 km but reaches a local maximum of 6 K around 95 km. The phase progressions are nearly continuous for all three waves in Figures 3d–3f, except at altitudes where wave amplitudes reach local minima. The vertical wavelengths derived from the linear fittings to the phase lines in the range of 40–110 km are around 51, 67, and 37 km for the 4-day, 2.5-day, and 1.7-day waves, respectively.

4. Discussion and Conclusions

The combined lidar and MLS temperature data provide, for the first time, observations of continuous and coherent vertical profiles of eastward propagating PWs from 30 to 110 km at McMurdo, Antarctica. Besides identifying a double-peak structure in the stratosphere and mesosphere, the observation shows a third dominant peak in the lower thermosphere (above 100 km). These results imply that there should be two peaks in geopotential from 30 to 110 km. As the thermospheric PW components are less likely to originate purely from direct wave propagation due to critical level dissipation, we apply the SD-WACCM data from 21 May to 1 June 2014 to examine their origins. The SD-WACCM has temporal and horizontal resolutions of 3 h and 1.9° × 2.5° (latitude × longitude) and is nudged at every 30 min with reanalysis data up to ~60 km (Kunz et al., 2011), which ensures that the model reproduces the dynamics and has no temperature biases in the troposphere and stratosphere.

We analyze the SD-WACCM data by first subtracting the data set temporal mean and then the zonal mean at each latitude and altitude to obtain perturbations. A two-dimensional fast Fourier transform is then applied to infer amplitudes and phases of the dominant waves (Lu et al., 2013). The 4dE1 wave is the strongest among waves with periods of 1–5 days. Figures 4a–4d show its amplitudes in geopotential height, temperature, zonal, and meridional winds. The latitudinal wave structure is consistent with the fact that this wave is highly confined to polar region, which has been shown in prior studies using SABER temperatures (Garcia et al., 2005) and reanalysis data (Lu et al., 2013) that have global coverage. Such a latitudinal structure is consistent with the fact that the wave source is associated with instability caused by the polar vortex, and it is difficult for PWs to propagate to equatorial regions due to critical level filtering (Lu et al., 2013). The vertical wave structure, that is, three peaks in temperature and correspondingly two peaks in geopotential height, is also qualitatively consistent with the observed 4-day wave amplitudes except for an underestimation above 100 km (Figure 3a). The amplitude peaks above the critical level are also found in zonal and meridional winds (Figures 4c and 4d).

Figure 4a shows that the local peaks below the critical level have downward tilt toward low latitudes, which closely follows the tilt of the critical level. The local peaks above it are more vertically aligned around 70°S extending to ~100 km. The local minima between these two peak regions also align well with the critical level. These features suggest that the dissipation of the stratospheric PWs is likely due to the critical level filtering. In the region with large wave amplitudes, wave phases generally have continuous vertical progressions (Figures 4e–4h), although the tilt of phase lines seems to alter from below to above the critical level (Figure 4e). An example is given for McMurdo (Figure 4i) where the phases in the four components generally show continuous progressions, especially above 50 km. In general, the SD-WACCM has qualitatively simulated the vertical and latitudinal structures of the 4dE1 wave and therefore is used for the following analyses. The meridional gradient of the PV $\left(\overline{q}_y\right)$ and the EP flux divergence $\left(\nabla\cdot\overrightarrow{F}\right)$ are calculated as equations (5.3.4) and (3.5.3) in Andrews et al. (1987):

$$\overline{q}_y = 2\Omega\cos\phi - \left[\frac{(\overline{u}\cos\phi)_\phi}{a\cos\phi}\right]_\phi - \frac{a}{\rho_0}\left(\frac{\rho_0 f^2}{N^2}\overline{u}_z\right)_z \tag{2}$$

$$\nabla\cdot\overrightarrow{F} = (a\cos\phi)^{-1}\frac{\partial}{\partial\phi}\left(F^{(\phi)}\cos\phi\right) + \frac{\partial F^{(z)}}{\partial z} \tag{3}$$

$$F^{(\phi)} = \rho_0 a\cos\phi\left(\overline{u}_z\overline{v'\theta'}/\overline{\theta}_z - \overline{v'u'}\right) \tag{4}$$

$$F^{(z)} = \rho_0 a\cos\phi\left\{\left[f - (a\cos\phi)^{-1}(\overline{u}\cos\phi)_\phi\right]\overline{v'\theta'}/\overline{\theta}_z - \overline{w'u'}\right\}, \tag{5}$$

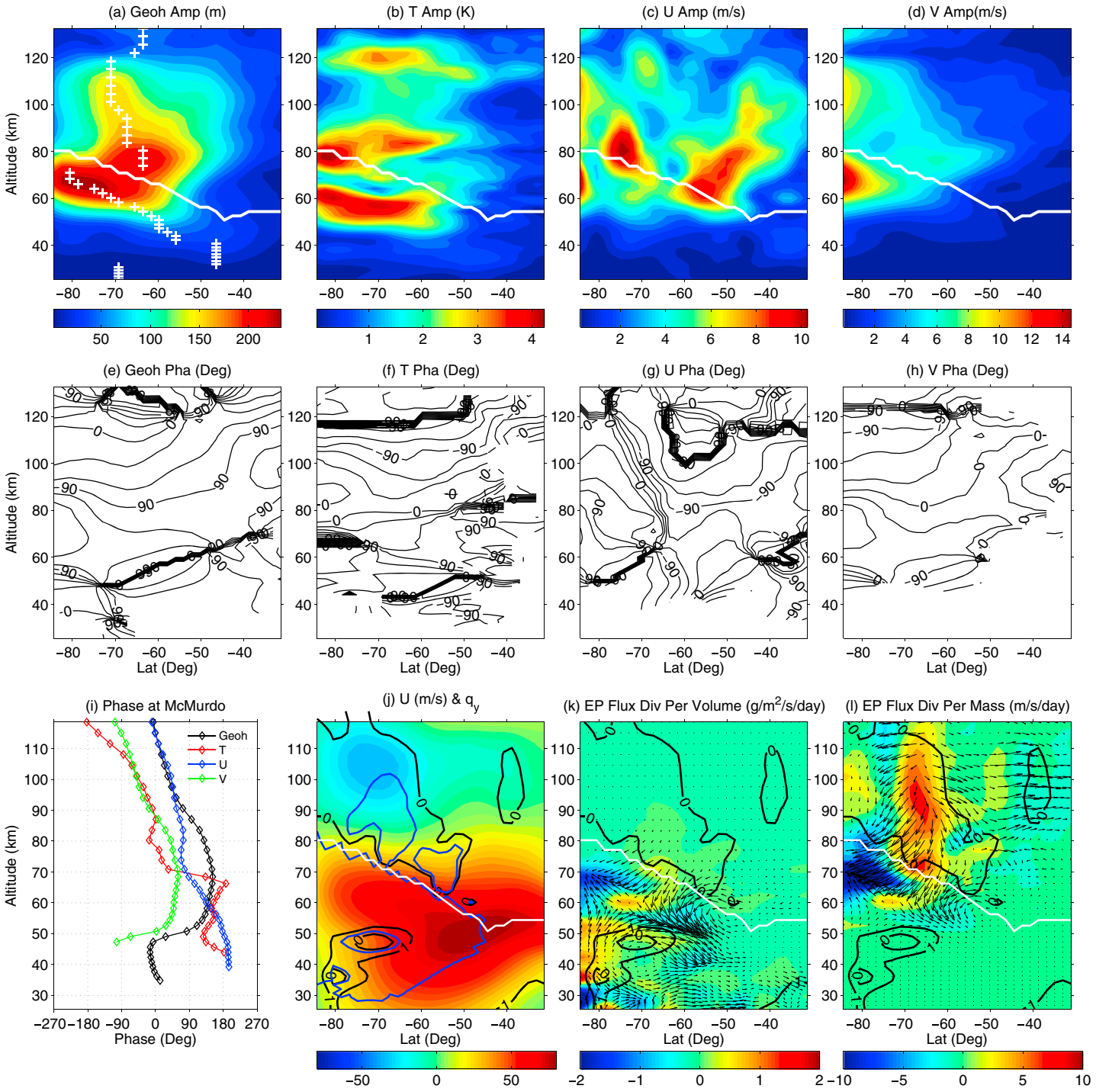

Figure 4. SD-WACCM 4dE1 wave amplitudes in (a) geopotential height (white pluses denote local maxima), (b) temperature, (c) zonal, and (d) meridional wind. (e–h) Same as Figures 4a–4d except for wave phases. The compacted contours are where phases change from −180° to 180°. (i) Wave phases at McMurdo. (j) $\overline{u}$ (color contours) and $\overline{q}_y$ (black contours). Blue contours encircle the regions with positive m^2. (k) EP flux divergence per unit volume $\left(\nabla\cdot\overrightarrow{F}/(a\cos\phi)\right)$ (contours) and vectors (arrows). The vertical vector has been multiplied by a viewing factor of 100. (l) EP flux divergence per unit mass $\left(\nabla\cdot\overrightarrow{F}/(\rho_0 a\cos\phi)\right)$. White lines in Figures 4a–4d and 4i–4k denote critical levels for 4dE1 wave.

where $F^{(\phi)}$ and $F^{(z)}$ represent the horizontal and vertical components of the EP flux; a and f are the Earth's radius and Coriolis parameter; ϕ and z are latitude and height; and u, v, θ, and ρ are zonal wind, meridional wind, potential temperature, and density, respectively. The EP flux divergence per unit volume is calculated as $\nabla \cdot \overrightarrow{F}/(a\cos\phi)$, and that per unit mass is $\nabla \cdot \overrightarrow{F}/(\rho_0 a\cos\phi)$ (McLandress et al., 2006).

Figure 4j shows the zonal mean zonal wind $\overline{u}$ and associated $\overline{q}_y$. The polar night jet is centered around 50°S and 50 km. Two regions with $\overline{q}_y < 0$ are identified: One is poleward of 60°S in the stratosphere and the other one with a tongue shape is in the MLT poleward of 50°S. Barotropic and baroclinic instabilities caused by the horizontal and vertical wind shears, respectively, are both important to produce negative $\overline{q}_y$. The EP flux divergences are shown in Figures 4k and 4l. Two main regions producing significant positive $\nabla \cdot \overrightarrow{F}$ are in the stratosphere poleward of 60°S and in the MLT centered around 65°S. It is clear that both regions of positive $\nabla \cdot \overrightarrow{F}$ which could indicate source regions (e.g., Chandran et al., 2013; Chang et al., 2011; Lawrence & Randel, 1996; Randel & Lait, 1991) are coincident with instability ($\overline{q}_y < 0$). Mechanistic models used to generate stratospheric PWs from the polar jet instability have also shown such coincidence (e.g., Hartmann, 1983; Manney & Randel, 1993). Therefore, similar coincidence above 60–70 km implies that the in situ instability in the MLT is likely another wave source.

The square of refractive index is determined as $m^2 = \frac{\overline{q}_y}{a(\overline{u}-c)} - \left(\frac{s}{a\cos\phi}\right)^2 - \frac{f^2}{4N^2H^2}$ (equation (7) in Lu et al., 2013). The notation follows the conventional meanings. $m^2 > 0$ favors wave propagation. Below the critical level, positive m^2 is found in the stable region ($\overline{q}_y > 0$) with negative intrinsic wave phase speed ($c - \overline{u} < 0$), while positive m^2 above the critical level (the two blue "ears" in Figure 4j) are found in the unstable region ($\overline{q}_y < 0$) with positive intrinsic phase speed $(c - \overline{u} > 0)$. This implies that once eastward PWs are generated/amplified in the MLT, they can propagate in the weak eastward or westward zonal mean winds when instability is present.

Combining the observations and SD-WACCM, we speculate the PW origin in the lower thermosphere as follows. The primary stratospheric PWs generated by the polar night jet instability are significantly damped around the critical level in the lower and middle mesosphere, which also hinders the direct free propagation. However, as long as the dissipation does not totally eliminate the waves and thus their magnitudes do not reduce to zero, the remaining wave disturbances can act as seeding perturbations. If such seeding penetrates to the unstable region in the MLT, amplification by instability can occur spontaneously. The in situ instability of the MLT is therefore important to cause an effective amplification of the remaining PWs. Once excited, the MLT winds are favorable for the wave propagation as long as the instability exists. The speculation of the "seeding-amplification" mechanism may explain the following two features: (1) Local peaks in geopotential, instability, and positive $\nabla \cdot \overrightarrow{F}$ are all coincident in the MLT. (2) Although the phase tilt alters, the phase lines below and above the critical level maintain certain continuity across the "barrier" of the critical level and appear not to be totally independent.

It is worth mentioning that although positive $\nabla \cdot \overrightarrow{F}$ correlates with instability spatially, we cannot fully rule out other possible wave sources such as the secondary PW generation by filtered GW forcing that has been proposed for stationary PWs (Lieberman et al., 2013; Smith, 1997, 2003), especially considering that SD-WACCM underestimates wave amplitudes above 100 km. The only wave dissipation considered in the stratospheric PW modeling is Newtonian cooling with a time scale of ~1/20 day^{-1} (e.g., Hartmann, 1983). In the MLT, eddy diffusion and momentum deposition from GWs are no longer negligible (Smith, 2003). In reality, how effectively the MLT in situ instability can amplify PWs should be determined by the competition of wave source and dissipation.

In summary, the eastward propagating PWs with periods of 1–5 days and wave numbers of 1–2 are observed continuously in a large vertical extension (30–110 km) over winter Antarctica for the first time. Temperature amplitudes show three main peaks, indicating the existence of a second geopotential peak in the MLT. The coherent vertical wave structure suggests a link between the stratospheric and MLT waves. The seeding-amplification mechanism of surviving PWs being amplified by in situ instability is speculated to explain these wave features with the aid of the SD-WACCM results.

Acknowledgments
We gratefully acknowledge invaluable discussions with Jens Oberheide, Kaoru Sato, and Hanli Liu on the wave analyses and dynamics. We appreciate the staff of the United States Antarctic Program, McMurdo station, Antarctica New Zealand, and Scott Base for their superb support. This work was supported by NSF grants OPP-0839091, OPP-1246405, and OPP-1443726. Xian Lu was supported by NSF/CEDAR grants AGS-1343106/1705448 and OPP-1543373/1705450. NCAR is supported by NSF, and WACCM is supported by NSF and the Office of Science of the U.S. Department of Energy. The data are available upon request.

References

Allen, D. R., Stanford, J. L., Elson, L. S., Fishbein, E. F., Froidevaux, L., & Waters, J. W. (1997). The 4-day wave as observed from the Upper Atmosphere Research Satellite Microwave Limb Sounder. *Journal of the Atmospheric Sciences*, *54*, 420–434. https://doi.org/10.1175/1520-0469(1997)054<0420:TDWAOF>2.0.CO;2

Andrews, D. G., Holton, J. R., & Leovy, C. B. (1987). *Middle atmosphere dynamics*. San Diego, CA: Academic Press.

Baumgaertner, A. J. G., McDonald, A. J., Hibbins, R. E., Fritts, D. C., Murphy, D. J., & Vincent, R. A. (2008). Short-period planetary waves in the Antarctic middle atmosphere. *Journal of Atmospheric and Solar-Terrestrial Physics*, *70*(10), 1336–1350. https://doi.org/10.1016/j.jastp.2008.04.007

Chandran, A., Garcia, R. R., Collins, R. L., & Chang, L. C. (2013). Secondary planetary waves in the middle and upper atmosphere following the stratospheric sudden warming event of January 2012. *Geophysical Research Letters*, *40*, 1861–1867. https://doi.org/10.1002/grl.50373

Chang, L. C., Palo, S. E., & Liu, H.-L. (2011). Short-term variability in the migrating diurnal tide caused by interactions with the quasi 2 day wave. *Journal of Geophysical Research*, *116*, D12112. https://doi.org/10.1029/2010JD014996

Chen, C., & Chu, X. (2017). Two-dimensional Morlet wavelet transform and its application to wave recognition methodology of automatically extracting two-dimensional wave packets from lidar observations in Antarctica. *Journal of Atmospheric and Solar Terrestrial Physics*, *162*, 28–47. https://doi.org/10.1016/j.jastp.2016.10.016

Chen, C., Chu, X., McDonald, A. J., Vadas, S. L., Yu, Z., Fong, W., & Lu, X. (2013). Inertia-gravity waves in Antarctica: A case study using simultaneous lidar and radar measurements at McMurdo/Scott Base (77.8°S, 166.7°E). *Journal of Geophysical Research: Atmospheres*, *118*, 2794–2808. https://doi.org/10.1002/jgrd.50318

Chen, C., Chu, X., Zhao, J., Roberts, B. R., Yu, Z., Fong, W., … Smith, J. A. (2016). Lidar observations of persistent gravity waves with periods of 3–10 h in the Antarctic middle and upper atmosphere at McMurdo (77.83°S, 166.67°E). *Journal of Geophysical Research: Space Physics*, *121*, 1483–1502. https://doi.org/10.1002/2015JA022127

Chu, X., Papen, G., Pan, W., Gardner, C. S., & Gelbwachs, J. (2002). Fe Boltzmann temperature lidar: Design, error analysis, and first results from the North and South Poles. *Applied Optics*, *41*(21), 4400–4410. https://doi.org/10.1364/AO.41.004400

Chu, X., Huang, W., Fong, W., Yu, Z., Wang, Z., Smith, J. A., & Gardner, C. S. (2011). First lidar observations of polar mesospheric clouds and Fe temperatures at McMurdo (77.8°S, 166.7°E), Antarctica. *Geophysical Research Letters*, *38*, L16810. https://doi.org/10.1029/2011GL048373

Chu, X., Yu, Z., Gardner, C. S., Chen, C., & Fong, W. (2011). Lidar observations of neutral Fe layers and fast gravity waves in the thermosphere (110–155 km) at McMurdo (77.8°S, 166.7°E), Antarctica. *Geophysical Research Letters*, *38*, L23807. https://doi.org/10.1029/2011GL050016

Coy, L., Stajner, I., Dasilva, A. M., Joiner, J., Rood, R. B., Pawson, S., & Lin, S. J. (2003). High-frequency planetary waves in the polar middle atmosphere as seen in a data assimilation system. *Journal of the Atmospheric Sciences*, *60*, 2975. https://doi.org/10.1175/1520-0469(2003)060<2975:HPWITP>2.0.CO;2

Fong, W., Lu, X., Chu, X., Fuller-Rowell, T. J., Yu, Z., Roberts, B. R., … McDonald, A. J. (2014). Winter temperature tides from 30 to 110 km at McMurdo (77.8°S, 166.7°E), Antarctica: Lidar observations and comparisons with WAM. *Journal of Geophysical Research: Atmospheres*, *119*, 2846–2863. https://doi.org/10.1002/2013JD020784

Fraser, G. J., Hernandez, G., & Smith, R. W. (1993). Eastward-moving 2–4 day waves in the winter Antarctic mesosphere. *Geophysical Research Letters*, *20*(15), 1547–1550. https://doi.org/10.1029/93GL01707

Garcia, R. R., Lieberman, R., Russell, J. M., & Mlynczak, M. G. (2005). Large-scale waves in the mesosphere and lower thermosphere observed by SABER. *Journal of the Atmospheric Sciences*, *62*(12), 4384–4399. https://doi.org/10.1175/JAS3612.1

Hartmann, D. L. (1983). Barotropic instability of the polar night jet stream. *Journal of the Atmospheric Sciences*, *40*(4), 817–835. https://doi.org/10.1175/1520-0469(1983)040<0817:BIOTPN>2.0.CO;2

Kunz, A., Pan, L. L., Konopka, P., Kinnison, D. E., & Tilmes, S. (2011). Chemical and dynamical discontinuity at the extratropical tropopause based on START08 and WACCM analyses. *Journal of Geophysical Research*, *116*, D24302. https://doi.org/10.1029/2011JD016686

Lawrence, B. N., & Randel, W. J. (1996). Variability in the mesosphere observed by the Nimbus 6 pressure modulator radiometer. *Journal of Geophysical Research*, *101*(D18), 23,475–23,489. https://doi.org/10.1029/96JD01652

Lawrence, B. N., Fraser, G. J., Vincent, R. A., & Philips, A. (1995). The 4-day wave in the Antarctic mesosphere. *Journal of Geophysical Research*, *100*(D9), 18899. https://doi.org/10.1029/95JD01168

Lieberman, R. S., Riggin, D. M., & Siskind, D. E. (2013). Stationary waves in the wintertime mesosphere: Evidence for gravity wave filtering by stratospheric planetary waves. *Journal of Geophysical Research: Atmospheres*, *118*, 3139–3149. https://doi.org/10.1002/jgrd.50319

Lu, X., Chu, X., Fuller-Rowell, T., Chang, L., Fong, W., & Yu, Z. (2013). Eastward propagating planetary waves with periods of 1–5 days in the winter Antarctic stratosphere as revealed by MERRA and lidar. *Journal of Geophysical Research: Atmospheres*, *118*, 9565–9578. https://doi.org/10.1002/jgrd.50717

Lu, X., Chu, X., Fong, W., Chen, C., Yu, Z., Roberts, B. R., & McDonald, A. J. (2015). Vertical evolution of potential energy density and vertical wave number spectrum of Antarctic gravity waves from 35 to 105 km at McMurdo (77.8°S, 166.7°E). *Journal of Geophysical Research: Atmospheres*, *120*, 2719–2737. https://doi.org/10.1002/2014JD022751

Manney, G. L., & Randel, W. J. (1993). Instability at the winter stratopause: A mechanism for the 4-day wave. *Journal of the Atmospheric Sciences*, *50*, 3928. https://doi.org/10.1175/1520-0469(1993)050<3928:IATWSA>2.0.CO;2

Manney, G. L., Orsolini, Y. J., Pumphrey, H. C., & Roche, A. E. (1998). The 4-day wave and transport of UARS tracers in the austral polar vortex. *Journal of the Atmospheric Sciences*, *55*, 3456. https://doi.org/10.1175/1520-0469(1998)055<3456:TDWATO>2.0.CO;2

Matsuno, T. (1970). Vertical propagation of stationary planetary waves in the winter Northern Hemisphere. *Journal of the Atmospheric Sciences*, *27*(6), 871–883. https://doi.org/10.1175/1520-0469(1970)027<0871:VPOSPW>2.0.CO;2

McLandress, C., Ward, W. E., Fomichev, V. I., Semeniuk, K., Beagley, S. R., McFarlane, N. A., & Shepherd, T. G. (2006). Large-scale dynamics of the mesosphere and lower thermosphere: An analysis using the extended Canadian middle atmosphere model. *Journal of Geophysical Research*, *111*, D17111. https://doi.org/10.1029/2005JD006776

Randel, W. J., & Lait, L. R. (1991). Dynamics of the 4-day wave in the Southern Hemisphere polar stratosphere. *Journal of the Atmospheric Sciences*, *48*(23), 2496–2508. https://doi.org/10.1175/1520-0469(1991)048<2496:DOTDWI>2.0.CO;2

Salby, M. L. (1982). Sampling theory for asynoptic satellite observations. Part II: Fast Fourier synoptic mapping. *Journal of the Atmospheric Sciences*, *39*, 2601–2614.

Sato, K., & Nomoto, M. (2015). Gravity-wave induced anomalous potential vorticity gradient generating planetary waves in the winter mesosphere. *Journal of the Atmospheric Sciences*, *72*(9), 3609–3624. https://doi.org/10.1175/JAS-D-15-0046.1

Scargle, J. D. (1982). Studies in astronomical time series analysis. II—Statistical aspects of spectral analysis of unevenly spaced data. *The Astrophysical Journal*, *263*, 835–853. https://doi.org/10.1086/160554

Schoeberl, M. R., Douglass, A. R., Hilsenrath, E., Bhartia, P. K., Beer, R., Waters, J. W., … DeCola, P. (2006). Overview of the EOS Aura mission. *IEEE Transactions on Geoscience and Remote Sensing*, *44*(5), 1066–1074. https://doi.org/10.1109/TGRS.2005.861950

Smith, A. K. (1997). Stationary planetary waves in upper mesospheric winds. *Journal of the Atmospheric Sciences*, *54*(16), 2129–2145. https://doi.org/10.1175/1520-0469(1997)054<2129:SPWIUM>2.0.CO;2

Smith, A. K. (2003). The origin of stationary planetary waves in the upper mesosphere. *Journal of the Atmospheric Sciences*, *60*(24), 3033–3041. https://doi.org/10.1175/1520-0469(2003)060<3033:TOOSPW>2.0.CO;2

Smith, A. K., Pedatella, N. M., Marsh, D. R., & Matsuo, T. (2017). On the dynamical control of the mesosphere-lower thermosphere by the lower and middle atmosphere. *Journal of the Atmospheric Sciences*, *74*(3), 933–947. https://doi.org/10.1175/JAS-D-16-0226.1

Wang, Z., Chu, X., Huang, W., Fong, W., Smith, J. A., & Roberts, B. (2012). Refurbishment and upgrade of Fe Boltzmann/Rayleigh temperature lidar at Boulder for McMurdo lidar campaign in Antarctica, *Proceeding of the 26th International Laser Radar Conference*, 207–210, Porto Heli, Greece, 25–29 June 2012.

Watanabe, S., Tomikawa, Y., Sato, K., Kawatani, Y., Miyazaki, K., & Takahashi, M. (2009). Simulation of the eastward 4-day wave in the Antarctic winter mesosphere using a gravity wave resolving general circulation model. *Journal of Geophysical Research*, *114*, D16111. https://doi.org/10.1029/2008JD011636

Zhao, J., Chu, X., Chen, C., Lu, X., Fong, W., Yu, Z., … Dörnbrack, A. (2017). Lidar observations of stratospheric gravity waves from 2011 to 2015 at McMurdo (77.84°S, 166.69°E), Antarctica: 1. Vertical wavelengths, periods, and frequency and vertical wave number spectra. *Journal of Geophysical Research: Atmospheres*, *122*, 5041–5062. https://doi.org/10.1002/2016JD026368